**Proceedings of the ASME 2009 International Design Engineering Technical Conferences &
Computers and Information in Engineering Conference
IDETC/CIE 2009
August 30-September 2, 2009, San Diego, USA**

DETC2009-87386

TOWARDS THE DESIGN OF A DECOUPLED, TWO-DIMENSIONAL, VISION-BASED μN FORCE SENSOR FOR MICROROBOTICS

David J. Cappelleri∗
Mechanical Engineering
Stevens Institute of Technology
Hoboken, New Jersey 07030
Email: David.Cappelleri@stevens.edu

Girish Krishnan
Mechanical Engineering
University of Michigan
Ann Arbor, Michigan, 48109
Email: gikrishn@umich.edu

Charles Kim
Mechanical Engineering
Bucknell University
Lewisburg, Pennsylvania, 17837
Email: charles.kim@bucknell.edu

Vijay Kumar
Mechanical Engineering and Applied Mechanics
University of Pennsylvania
Philadelphia, Pennsylvania, 19104
Email: kumar@seas.upenn.edu

Sridhar Kota
Mechanical Engineering
University of Michigan
Ann Arbor, Michigan, 48109
Email: kota@umich.edu

ABSTRACT

In this paper, we present three designs for a decoupled, two-dimensional, vision-based μN force sensor for microrobotic applications. There are currently no reliable, off-the-shelf, commercially-available force sensors to measure forces at this scale, that can be easily integrated into standard microrobotic test-beds. In our previous work, we presented a design consisting of a planar, elastic mechanism with known force-deflection characteristics. It was inspired by the designs of pre-existing MEMS suspension mechanisms. A CCD camera is used to track the deformation of the mechanism as it is used to manipulate objects in a micro/meso-scale robotic manipulation test-bed. By observing the displacements of select points in the mechanism, the manipulation forces can be estimated. Here, a building block approach for conceptual synthesis of compliant mechanisms methodology is used to design for decoupled displacements for the tracking points when the tip is subjected to forces in the XY-plane. By designing mechanisms with circular compliance and stiffness ellipses along with zero magnitude compliance and stiffness vectors, we are able to achieve our design requirements. Validation of this approach with macro-scale prototypes and recommendations for scaling the designs down for microrobotic applications are offered along with a sensitivity analysis of the final designs yielding insights for microfabricating such designs.

∗Address all correspondence to this author.

INTRODUCTION

The real advantages of a high precision microrobot or manipulation system can only be utilized if the automated system also has high resolution sensors along with good control strategies [10]. Force sensors capable of resolving micro-Newton (μN) level forces, the typical forces encountered when manipulating biological cells and micro- and meso-scale parts, are generally made using microfabrication techniques. The traditional methods of indirect force measurements, like mounting strain gauges at specific locations [13, 28, 30] is hard to demonstrate at the MEMS scale because it substantially complicates the micro-fabrication process. Methods like capacitance-based indirect force measurement usually require special electronic circuitry to measure the low capacitance of femto- and atto-farads and thus a complicated microfabrication process [2,9,26,27] that can drive up production costs. Indeed there are no commercially-available, inexpensive, multi-axis force sensors at this scale that can be easily integrated into a typical micromanipulation system. Our goal is to come up with a design that can be easily integrated into a microrobotic test-bed like the one shown in Figure 1 [4,6,7], which does not require any alteration of the object being manipulated or require exotic fabrication techniques and can sense μN level forces in two dimensions. With such a design, real-time controlled manipulation of micro-objects is possible. In this paper, we develop an optimal, decoupled, two-dimensional, computer vision-based, force sensing device which consists of an elastic mechanism with known force-deflection characteristics. From observing the deformation of a calibrated structure as it interacts with an object that it is manipulating, the actual
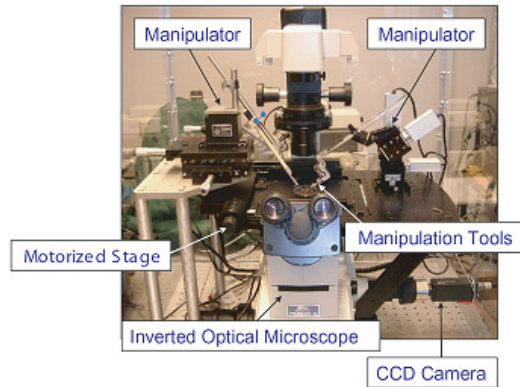
Figure 1. MICROROBOTIC TEST-BED

manipulation force can be extracted. The design for the compliant mechanism consisting of the device is synthesized utilizing a combination of serial and parallel concatenation of compliant building blocks.

RELATED WORK

The development of micro-force sensors is an active research area. An overview of force sensing for microassembly applications using capacitance, optical, piezoelectric, piezoresistive, SFM (scanning force microscope), AFM (atomic force microscope), and laser Raman spectrophotometer (LRS) techniques is given in [21]. A review of MEMS devices used for cellular force measurements can be found in [25], while a more general summary of micro-force sensor research is presented in [4]. The commercially available force sensor AE 801 Micro Force Sensor from SensorOne (*http://sensorone.com*) can measure forces from 12 grams down to 12 mg (118 mN to 118 μN) in one dimension. An AFM is commonly used to measure smaller forces, in the pN to nN range. A very detailed description of the various techniques, interpretation and applications of force measurements with an AFM is given in [3]. Sitti et al. used an AFM for manipulation along with integrated force sensing at the mN level in [24]. Koch, et al. [17] designed, fabricated, and tested a compliant surface-micromachined spring in order to calibrate the lateral force field of an electromagnet on a single magnetic microparticle. Due to the high resolution microscope objective used, pN force sensitivity is achieved. The Zyvex Force Characterization Package (FCP) (*http://www.zyvex.com*) is capable of measuring one dimensional forces ranging from nN to mN but requires extensive (proprietary) hardware, software, as well as a high resolution scanning electron microscope to function.

In regards to vision and optical force sensing, the design for a micrograting-based force sensor integrated with a surface micromachined silicon-nitride probe for penetration and injection into drosophila embryos is presented in [31,33]. Penetration forces in the μN range have been recorded and the device has also been used to characterize positioning forces on the drosphilia embryos that are self-assembled in 2-D arrays [32]. Optics are also used in [34] and [14] to sense contact forces. A minimally intrusive, vision-based, computational force sensor for elastically deformable objects is presented in [29]. Force estimation is calculated from the visually measured displacements and known material properties of the deformable object. This approach is only viable if the displacements of the deforming object can be captured accurately. Greminger, et al. demonstrates a method to

visually measure the force distribution applied to a linearly elastic object using the contour data in an image in [11]. A sensor resolution of less than $\pm$ 3 nN for a microcantilever and $\pm$ 3 mN for a microgripper were achieved. Sasoglu, et al. have used high-aspect ratio polydimethylsiloxane (PDMS) microbeams to sense one dimensional micro-scale forces specifically targeted for single cell studies [23]. Similar PDMS beam structures have been used by Liu et al. [20] to hold a cell in place during microrobotic mouse embryo injection while tracking the beam displacements, thus extracting force information. A sub-pixel visual tracking algorithm allows for 3.7 nN force resolution.

In our previous work [4, 5], we have presented a design that allows for two-dimensional sensing of micro-forces and that can be easily integrated into standard robotic manipulation test-beds without cluttering the workspace or requiring any complicated drive electronics (Figure 2). It can also be used as a manipulation tool to execute a variety of tasks and has many different applications. The design topology was inspired by traditional MEMS suspension mechanisms found in accelerometers and resonators with the final geometries selected based on a Monte-Carlo method optimization routine. They were microfabricated out of polydimethylsiloxane (PDMS) material. Other materials such as silicon and soft metals (copper, beryllium copper) were initially considered for the force sensor. However, in order to produce device stiffnesses sensitive enough to resolve μN forces with these materials, designs with very large length-width aspect ratio beams were required which caused the device to buckle under it's own weight. The designs were also too large to have a sufficient portion of them reside in the field of view of the microscope. Choosing PDMS for the device allows for a much smaller device footprint along with a larger minimum feature size and thus easier manufacturing. The manufacturing process consists of an initial photolithography process with a thick photoresist to create a mold of the desired part geometry in the photoresist, PDMS pouring and curing inside the mold, followed by a wet etching step to plane the PDMS. The photoresist mold is then dissolved and the parts extracted from the substrate. These devices exhibited coupled displacements (in the plane) of the tracking points when subjected to transverse and off-axis loading, which can lead to difficulties in accurately resolving the two force components at the tip. In this paper, we present next generation designs for our 2-D vision-based force sensors, designed for decoupled motions. A building block approach [15, 18] for conceptual synthesis of compliant mechanisms methodology is used to design for the decoupled displacements for the tracking points when the tip is subjected to forces in the XY-plane. Macro-scale prototype testing is also presented, validating this methodology, and recommendations for scaling the designs down for microrobotic applications offered along with some conclusions.

FORCE SENSOR SPECIFICATIONS

The specific performance specifications for the force sensor are dictated by the constraints imposed by the vision system in the microrobotic test-bed and particular application. A probing section of the force sensor mechanism with tracking points along with a fixed, stationary point need to be in the microscope field of view (FOV) at all times so they can be observed by the CCD camera and displacement information extracted and converted to manipulation forces using the device's stiffness calibration data. The constraints imposed by the vision system are dependant on the choice of microscope objective. For example, when using the 4X objective in our system the size of the FOV is 3.368 mm $\times$ 2.626 mm, with an image resolution of 5.26 μm/pixel. However,
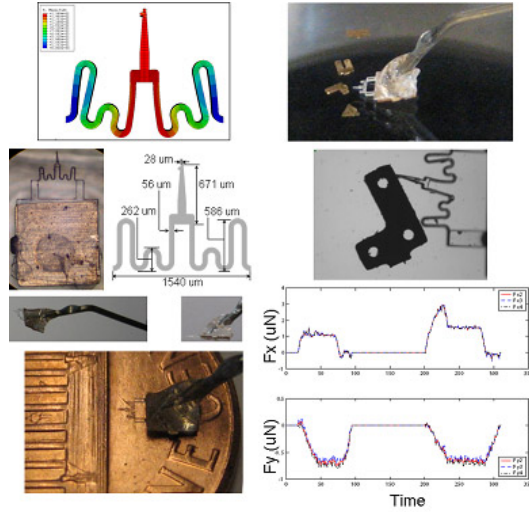
Figure 2. 2-D VISION-BASED FORCE SENSORS

Table 1. DESIGN SPECIFICATIONS PER APPLICATION AREA

	Meso/micro-scale Assembly	Cell Manipulation
Expected Force Range	0 to 50 μN	0 to 10 μN
Characteristic Length	1200 μm $\times$ 500 μm	50 μm to 200 μm diameters
Objective	4X	40X
Desired Resolution	0.25 to 0.75 μN/pixel	0.01 to 0.05 μN/pixel
XY Stiffness Range	0.05 to 0.15 N/m	0.025 to 0.100 N/m
Maximum Deflection	200 μm	20 μm

with a 40X objective, the FOV reduces to 344 μm $\times$ 258 μm, with a corresponding image resolution of 0.537 μm/pixel. (Note: the accuracy of the vision-based force sensor is not necessarily equal to the image resolution. Rather, it corresponds to the robustness and accuracy of the feature tracking algorithm utilized.)

Two initial application areas are considered when designing these vision-based force sensors: meso/micro-scale assembly and biological cell manipulation. The design specifications for each of these are listed in Table1. In the case of meso/micro-scale assembly, large deflections ($\geq$ 1 pixel = 5.26 μm) are required to be able to optically track them with the camera. The larger objective and corresponding FOV that is used with cell manipulations will require much smaller deflections to be observed. The maximum deflection values listed in the table are the maximum deflection allowed for the device to keep all necessary tracking points in the FOV during a particular type of manipulation. Thus, the range for the designed sensor will be it's XY stiffness $\times$ this maximum deflection value. The desired resolution ranges for each of the applications are 0.25 - 0.75 μN/pixel and 0.01 - 0.05 μN/pixel, respectively. This, along with the image resolution for the particular objective being used, determines the acceptable XY stiffness range for the force sensor. As stated previously, capacitive and piezoresistive strain gage MEMS sensors are capable of achieving similar resolutions but suffer from complicated manufacturing processes and require special drive electronics for operation. The advantages to our vision-based force sensor designs are that they can be easily integrated into standard microrobotic testbeds without the addition of this extra hardware, do not have a complicated fabrication process, and can sense forces in two-dimensions while also being used as a manipulation tool.

The main objective for the problem at hand is to design a compliant force sensor which has equal stiffness in $X-$ and $Y-$ direction. An equal stiffness design allows for easier force extraction from the observed displacements of the device and uniform performance in each planar direction. In applications that may require unequal stiffnesses, the same methodology shown here may also be applied. Previous attempts to design a compliant force sensor with equal stiffness were inspired by MEMS based suspension designs. These designs were optimized to ob-

tain the required sensitivity and stiffness specifications in both directions. The resultant designs suffered from off-axis coupling, also known as the parasitic error. For example, force along the $X-$ axis caused displacements along both the $X-$ and $Y-$ directions and also caused a slope (or rotation) at the input. Furthermore, the sensitivity of the designs to geometry variations was not studied. In the present work, we aim to systematically design the compliant members by directly translating the general problem specifications to quantities that characterize the deformation of the compliant member. The general problem specifications include

1. Equal X and Y stiffness.
2. Completely decoupled X and Y translations.
3. Rotation about the Z axis should be independent of the translations and forces.

The resultant of such a systematic characterization was the decomposition of the problem specification into simpler objectives. These are readily achieved, either from a library of building blocks or by a systematic combination of a number of building blocks.

FORCE SENSOR DESIGN

In this section, we aim to achieve the problem specifications put forth for the sensor. This involves translating the problem specification to quantities that directly define the geometry of the mechanism. We use the eigen-twist and eigen-wrench parameters for 2-D complaint members to characterize the compliance and the stiffness matrix. We then simplify the problem specification into simpler sub-problems, solve them and combine the subproblems with modifications to suit the application. This design process is described in the following sections.

Characterization of deformation for a compliant mechanism

The nature of deformation for a compliant mechanism can be characterized by its compliance matrix. The compliance matrix gives a relationship between the forces and moments, and the degrees of freedom. For a 2-D planar compliant member, there are three degrees of freedom at a point, namely two translations and a rotation about an out of plane axis passing through the point. The compliance matrix has terms involving rotations and translations intricately coupled [18]. Thus for effective characterization, it is required to decouple these terms. This can be effectively accomplished by shifting the point of interest to a point away from the input, where any force applied gives pure translation alone and any moment applied gives a pure rotation [16]. Such a point is called the center of elasticity (CoE) and is shown to be unique for a 2-D elastic body under a particular set of loading conditions [19]. In a 2-D setup, the center of elasticity is co-
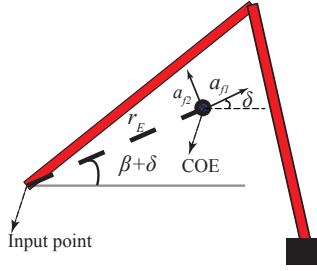
3

Figure 3. EIGEN-TWIST AND EIGEN-WRENCH PARAMETERS FOR A COMPLIANT DYAD BUILDING BLOCK.

Figure 4. a) COMPLIANCE ELLIPSE b) COMPLIANCE COUPLING VECTOR (C_m) c) STIFFNESS ELLIPSE d) STIFFNESS COUPLING VECTORS (S_m)

incident with the center of stiffness as defined in precision mechanism design [1, 12], remote center of compliance [RCC] as defined in robotics [8, 22], and the elastic center [8] where the stiffness and compliance matrix can be diagonalized. In this paper, we will refer to the point as the center of elasticity as we obtain it by the application of eigen-twist eigen-wrench [19] characterization to the 3×3 matrix. Thus, the parameters of interest for these eigen-twist and eigen-wrench entities are shown in Figure 3. The eigen-twist and eigen-wrench parameters (a_{f_1}, a_{f_2}, k_g, r_E, β, and δ) can be divided into three main categories

1. Translational Compliance: Given by a_{f_1} and a_{f_2} , these eigen-compliance parameters depict semi-major and semi-minor axes of translational compliance as observed from the center of elasticity. We denote $n_p = a_{f_2}/a_{f_1}$ as the ratio of the semi-minor axis to the semi-major axis of the eigen-complaince ellipse.
2. Eigen-rotational Stiffness (k_g) : This gives the reaction moment produced by a pure unit rotation at the center of elasticity
3. Center of elasticity: Its distance (r_E) and orientation (β) with respect to the point of input indicates the coupling that exists between rotational and translational parameters. It must be noted that β is the orientation of the center of elasticity with respect to the horizontal only when the a_{f_1} - a_{f_2} axes are aligned along the $X - Y$ axes. δ is the orientation of the semi-major axis of the ellipse (a_{f_1}) with respect to the horizontal.

The compliance matrix can be represented by an ellipse whose semi-major axis is a_{f_1} and semi-minor axis is given by a_{f_2} as shown in Figure 4. The coupling terms which denote the displacements due to moments can be represented as a vector known as a compliance coupling vector (C_m). Similarly, the stiffness matrix can be represented as an ellipse whose semi-major axis is $1/a_{f_2}$ and semi minor axis is $1/a_{f_1}$. The magnitudes of the compliance vector, and the stiffness coupling vector (S_m) are shown in Eq. 1-2. The orientaiton of the stiffness coupling vector (S_m) is given by $\beta+\delta+\gamma$, where γ is given in Eq.3.
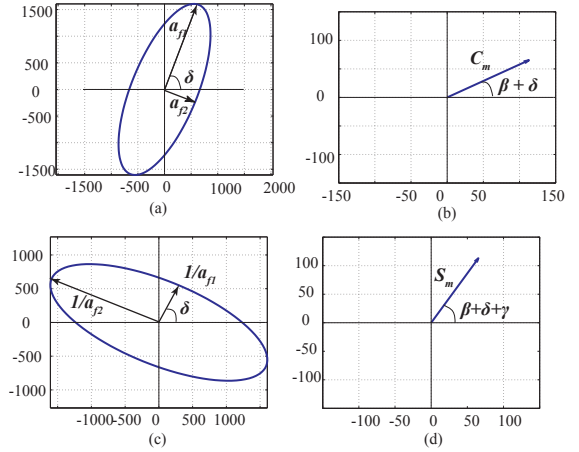
$$C_m = \frac{r_E}{k_g} \tag{1}$$

$$S_m = \frac{2r_E}{a_{f_1}} \left(\frac{1}{n_p^2} \cos^2 \beta + \sin^2 \beta \right) \tag{2}$$

$$\gamma = tan^{-1} \frac{1 - n_p}{(1 - n_p)\cos 2\beta + (1 + n_p)} \tag{3}$$

Problem specification in terms of the eigen-twist and eigen-wrench parameters

In this section, we translate the problem specification into eigen-twist and eigen-wrench parameters.

1. Equal Stiffness in the *X* and *Y* directions: This means that the stiffness and the compliance matrix are diagonal, with $a_{f_1} = a_{f_2}$ or n_p =1. Graphically, this means that the compliance and the stiffness ellipses are now circles, with radii a_{f_1} and $1/a_{f_1}$ respectively.
2. Decoupling the effects of translation and rotations: This implies that the stiffness and the compliance coupling vectors have zero magnitude (C_m=0, S_m=0). This further means that the center of elasticity is at the input point (r_E=0). Similar specifications have been earlier reported in the design of flexure based precision mechanisms [1, 12], and in the RCC devices [22].

To simplify this problem specification, we restrict our attention to symmetric mechanisms. Adding mechanisms in parallel adds the stiffness coupling vector (vectorially) and the stiffness ellipses of the individual building block.This implies that the stiffness-coupling vector of the symmetric halves should be equal in magnitude and opposite in direction. Furthermore, to obtain equal *X* and *Y* stiffness, the stiffness ellipse (and thus the compliance ellipse) we desire the ellipses of the symmetric halves to be a circle. Then as given by Eq. 3, $\gamma = 0$. This means
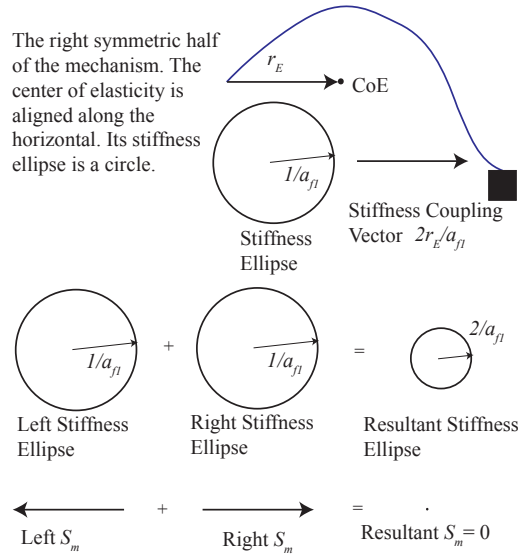
4

Figure 5. PROBLEM SPECIFICATION FOR THE FORCE SENSOR AS-SUMING THE MECHANISM TO BE MADE UP OF TWO SYMMETRIC HALVES.

Figure 6. DIFFERENT DESIGNS FOR THE SYMMETRIC HALF OF THE MECHANISM WITH EQUAL STIFFNESS IN THE $X-$ AND $Y-$DIRECTIONS. (a) ONE BUILDING BLOCK, (b) TWO BUILDING BLOCKS c) MULTIPLE BUILDING BLOCKS.

Figure 7. ASSEMBLED SYMMETRIC MECHANISM WITH INPUT AT THE CENTER OF ELASTICITY.

that the stiffness and the compliance coupling vectors C_m and S_m have the same orientation. These specifications are illustrated in Figure 5.

Thus the problem specification can be divided into three stages

1. Design the symmetric half of the mechanism whose compliance (and thus stiffness) ellipses are circular ($a_{f_1} = a_{f_2}$).
2. Rotate the halves so that their coupling vectors are along the horizontal ($\beta + \delta = 0$ or $180°$).
3. Combine the symmetric halves to obtain the resultant mechanism.

The resultant mechanism will thus have equal stiffness and have its input at the center of elasticity (thus decoupling translations and rotations). In the next section, we briefly explain the design of the symmetric half of the mechanism.

Designing the symmetric half using building block method

The building block approach [15] to obtain single point compliant mechanisms was used to obtain the symmetric half of the force sensor. In this approach, the given problem specification is decomposed into tractable sub-problems. Simple deformable members (building blocks) such as a single beam or a dyad are used as solutions to sub-problems, which when combined (in series or in parallel) help satisfy the overall problem specification. For the problem in hand we try to obtain designs by series concatenation of building blocks. Series combination of flexures have been commonly used in analyzing flexure based mechanisms by Hale [12]. It involves the addition of compliance matrices of the individual building blocks. In our methodology, we use graphically intuitive compliance ellipses and coupling vectors to
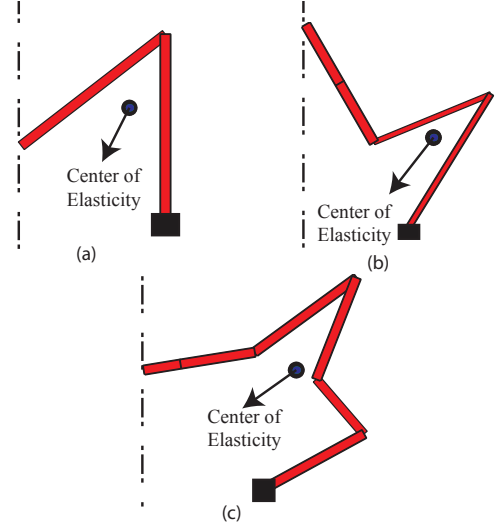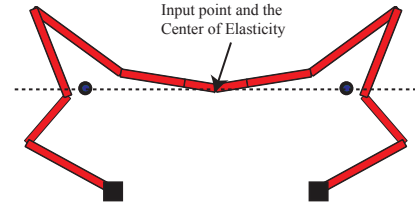
combine standard building blocks such as dyads and beams in series. The coupling vectors and ellipses add in series, with some modifications. We choose the appropriate building blocks whose coupling vectors and ellipses add to give the required compliance specifications. Details of the design methodology is given in [18].

It was seen that a single dyad (Figure 6(a)) was able to satisfy the specifications of equal stiffness in both directions. However, to evaluate and compare better designs in terms of the mechanism footprint and other specifications, we specify other designs which are obtained by series concatenation of building blocks, as shown in Figures 6(b) and (c). We chose the third design for further analysis, as its compliance ellipse was least sensitive to slight geometric variations. This sensitivity analysis is presented later in our *Discussion* section.

Combination of the symmetric halves and modifications

The symmetric halves for the mechanism were rotated so that their centers of elasticity (or coupling vectors) were inclined along the horizontal and combined to form the full design for the mechanism, as shown in Figure 7. During micro-manipulation of minute objects, it is not possible to directly apply force on the input point. There is a necessity of a pointer, which is rigid and
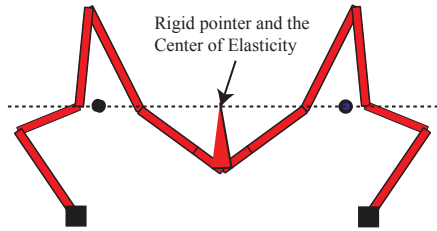
5

Figure 8.   MODIFIED DESIGN WERE THE SYMMETRIC HALF OF THE MECHANISM IS FURTHER ROTATED TO ACCOMMODATE THE RIGID POINTER.
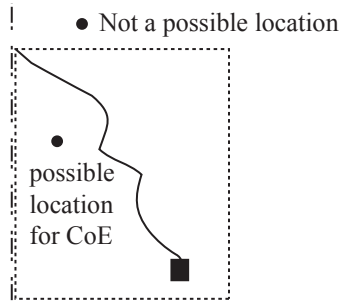

Figure 9.   THE CENTER OF ELASTICITY IS BOUNDED BY THE FOOT-PRINT OF THE MECHANISM [18].

Figure 10.   MODIFICATIONS OF THE DESIGN FOR THE TWO POINT SENSING STRATEGY.

does not contribute to the overall compliance of the mechanism. However, adding a rigid body at the input does not change the compliance magnitudes, and keeps the absolute position of the center of elasticity the same. To accommodate a rigid pointer, the symmetric half of the mechanism was further rotated so that the center of elasticity lies in the same line as the end of the rigid pointer, as illustrated in Figure 8.

It can also be seen in Figure 8 that the workspace for the mechanism is limited by the length of the pointer and the interference between the parts of the mechanism on either side of it. Thus arises a need to obtain a symmetric half with its center of elasticity lying beyond its footprint. However, it is proved in [18] that such a solution is not possible. The center of elasticity for series combination of building blocks always lie within the footprint of the mechanism as shown in Figure 9. Thus, to eliminate the problem of interference, we propose a two-point sensing strategy. In this, we use the pointer to manipulate the object, but sense the deflection at the center of elasticity which is different from the point of input. In this case the mechanism has equal X and Y stiffness at the center of elasticity, and not at the input. Figure 10 shows the modified design using this type of sensing strategy.

Final designs for prototyping and experimentation

Using the methodology described, three final designs for prototyping and experimentation were created and are shown in Figure 11. The first design (Figure 11(a), as discussed in the previous section, makes use of a rigid pointer. The symmetric halves are rotated so that the their individual centers of elasticity are horizontally aligned with the end of the pointer. As explained previously, this design suffers from limited workspace due to interfering regions of the mechanism. The second design
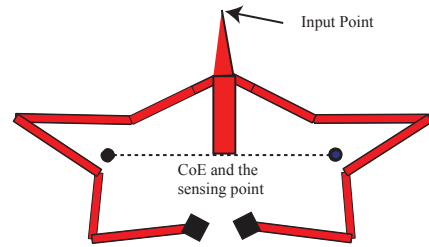
(Figure 11(b) illustrates the concept of sensing away from the point of input. Here, the force is applied along the pointer, while the point being sensed is along the center of elasticity. The center of elasticity for this design is at the center of the arc. It must be noted that for this design, the stiffness is measured by dividing the force applied at the input (i.e. tip of the pointer) by the displacement at the center of elasticity. The final design (Figure 11(c) uses the same concept of the first design. The region around the input is made spacious (less obstructed) by adding a larger, centrally located rigid body. It must be noted that adding this region does not affect the eigen-compliances and the absolute location of the center of elasticity. The center of elasticity is located at the input. Figure 12 gives the FEA deformation of these three final designs. For designs 1 and 3, where the input is at the center of elasticity, we observe negligible rotation at the input point for forces in $X-$ and $Y-$ direction. In all the designs shown in Figure 11, the in-plane thickness and the out-of-plane thickness values are uniform. They can thus be uniformly scaled to be suitable for micro-scale applications. In the later sections, we show that the relative thickness of the deformable members along with the variations in the geometry affect the performance of the mechanism.

EXPERIMENTS

In order to verify the methodology used for force sensor designs presented above without the rigors of the microfabrication process, described in [5], the three final design geometries were scaled to the macro-level for fabrication and testing. The designs were scaled so that the minimum beam width dimensions in each equaled 1 mm (0.0394"), with the rest of the geometry scaling accordingly. The prototypes were manufactured with a 50-Watt laser cutter (X-660 from ULS, Inc.) out of Lucite CP acrylic sheets, approximately 1/8" thick. The sharp pointers at the input points of the designs were flattened in the manufactured prototypes for ease in testing. Scale-bars have also been added (etched) along the rigid pointer sections, spaced 1 mm apart, for use in the device calibration. These macro-scale, prototypes are shown in Figure 13.

Calibration Experiments

The experimental testing setup for the stiffness calibration tests on the prototypes is shown in Figure 14.   A compression-type load cell (GS0-10 from Transducer Techniques, *www.transducertechniques.com*) is mounted to a 2-axis linear translation stage (Edmund Optics 5" Square Translation Stage, *www.edmundoptics.com*).   The output of the load cell is routed through a voltage amplifier (Entran IMV-15/10/100A-
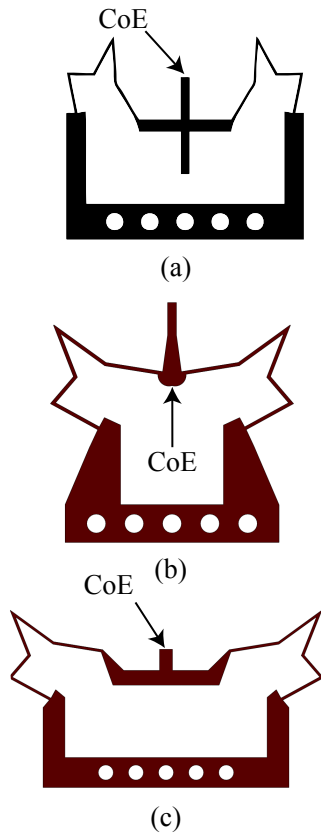
6

Figure 11.   FINAL DESIGNS USED FOR PROTOTYPING.

Figure 12.   DEFORMATIONS FOR X AND Y FORCES FOR (a) DE-SIGN 1, (b) DESIGN 2, AND (c) DESIGN 3.

WW, *www.entran.com*) and then to a data acquisition card on a PC. A DC tracking power supply (Leader LPS 151, *www.leaderusa.com*) is used to power the amplifier and load cell. The prototypes are fixed to a mount with the mounting holes designed into their respective frames. The mount is placed in one of two configurations: it is oriented either in-line with or at a 90° angle to the load cell, in order to measure the stiffness in the either the vertical (Y-axis) or horizontal (X-axis) directions, respectively. A custom-made L-shaped adapter bracket is fixed to the load cell stem to allow for flush contact between the load cell and prototype tip during each test. A fixed displacement of the prototype tip is applied by turning a knob on the translation stage that the load cell is mounted to. The corresponding force for this displacement is then recorded. At least three vertical and horizontal test trials were conducted on each of the prototypes under investigation. Images of the starting, maximum displacement (load), and final configurations were captured with an overhead camera. The images were analyzed off-line to determine the actual displacements for the theoretical CoE position when subjected to a particular load. Initially, images of the load cell adapter bracket before and after a 2 mm displacement were used to determine the image resolution, i.e. the pixel-to-mm conversion factor, for each test. In each trial, the offset between the tracking point (CoE) and a fixed point on the prototype (one that does not move with applied forces) is calculated for each image and compared to determine the maximum displacement of the CoE for that particular trial. The experimental stiffness is calculated for each trial as the ratio of the maximum recorded force
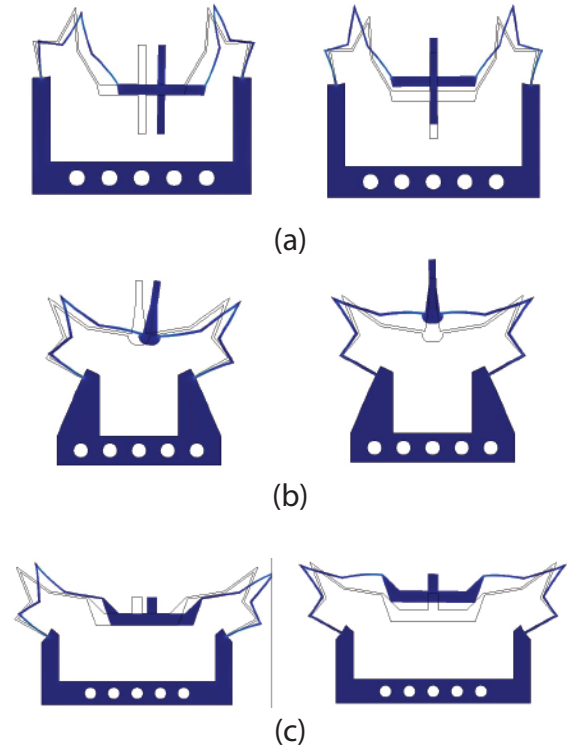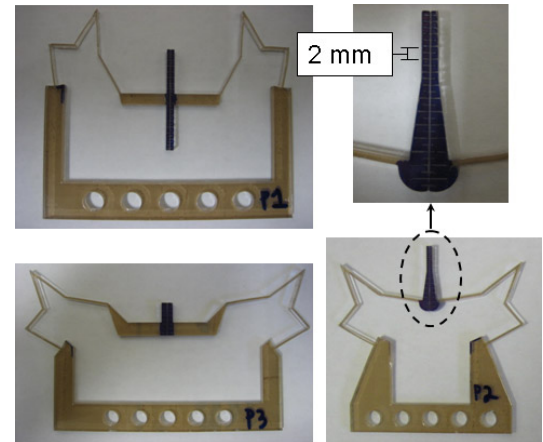

Figure 13.   SCALED PROTOTYPES

and this corresponding maximum displacement of the CoE of the prototype. The stiffness value for a particular prototype and direction is then taken as the average of the stiffness values across all the trials. The results from these calibration tests are shown in Table 2 compared with their corresponding FEA software predicted values, using $E_{acrylic} = 2.65$ GPa and $v_{acrylic} = 0.41$. The differences between the experimental and FEA predicted stiffness values are all less than 10%.

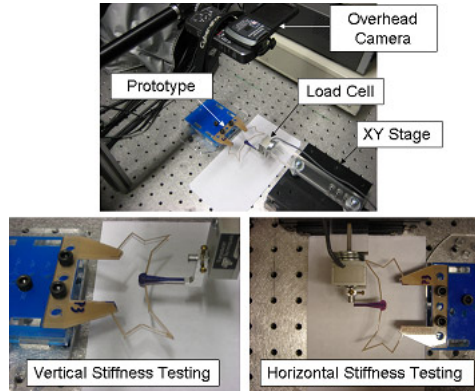For decoupled motions, one would expect that the stiffness

7

Figure 14. EXPERIMENTAL TESTING SETUP

in each direction are identical. Indeed, the experimental results from Prototypes 1 and 3 yield stiffness ratio values, K_y/K_x, close to 1 (0.95 and 0.83, respectively) and in agreement with the FEA predicted stiffness ratios. The stiffness ratio for Prototype 2 is slightly less than predicted, (0.73 vs 0.84). Reasons for this discrepancy as well as reasons for the variation of the stiffness ratio from the ideal value of 1.0 will be explained in our *Discussion* section.

Table 2. PROTOTYPE STIFFNESS COMPARISON

|	FEA			Exp.		
Prototype	K_x (N/m)	K_y (N/m)	K_y/K_x	K_x (N/m)	K_y (N/m)	K_y/K_x
P1	156	156	1.00	170	161	0.95
P2	317	268	0.84	337	245	0.73
P3	178	147	0.83	174	145	0.83

Manipulation Experiments

Manipulation experiments were performed using Prototype 2. The prototype base was mounted to the XY stage in such a way to allow the rigid probe section to be cantilevered off the front of the stage. The stage was translated to apply horizontal and vertical test pushes against an object of interest and the forces required to move it from rest extracted. Screen shots from test pushes are shown in Figure 15. As in the case of the calibration experiments, images of the prototype before and during the manipulation tasks were analyzed off-line to determine the actual displacements for the CoE position when force is applied to the tip of the device. The displacements were then converted to manipulation forces by multiplying them by the prototype stiffness value in the corresponding direction. In the case of the vertical manipulation test pushes, the vertical displacement of 2.38 mm is multiplied by $K_y = 245$ N/m to yield a manipulation force of 583 mN, while in the case of horizontal test push, the displacement of 1.59 mm $\times$ 337 N/m corresponds to a force of 536 mN to move the object from rest.

DISCUSSION

The FEA analysis predicts the stiffness values of the prototypes quite well. However, there are some differences from the
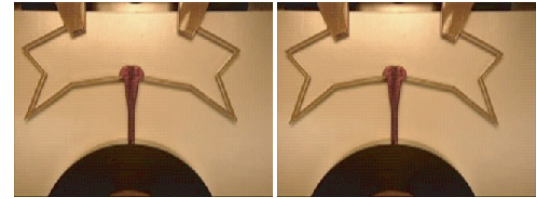
(a) Vertical push: Undeformed (L) and deformed (R) configurations
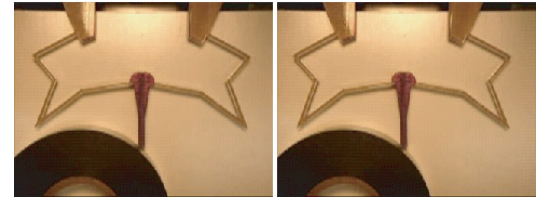
(b) Horizontal push: Undeformed (L) and deformed (R) configurations

Figure 15. SNAPSHOTS FROM MANIPULATION TESTS

Table 3. PROTOTYPE BEAM AND PART THICKNESS RANGES

Prototype	In-Plane Beam Thickness	Out-of-Plane Part Thickness
P1	0.0252" - 0.0327"	0.1185" - 0.1220"
P2	0.0398" - 0.0472"	0.1182" - 0.1225"
P3	0.0344" - 0.0454"	0.1198" - 0.1267"

idealized stiffness ratio values that they were designed for. These differences can be explained by the following.

1) Variation of the prototype in-plane and out-of-plane thickness values due to manufacturing errors.

The in-plane thickness of the beams are designed to be around 1 mm. The stiffness is dependent on the cube of the beam thickness, and hence a small variation can cause a large error. For a thickness of 1 mm, the stiffness predicted is around 130 N/m, but with 2 mm the stiffness predicted is around 1200 N/m, which is an increase of around 8$\times$. Thus the accuracy of the beam thickness from fabrication is important. However, a uniform error on the thickness still gives equal X and Y stiffness of the mechanism and does not change the position of the center of elasticity. By measuring the in-plane thickness of the beams on the prototypes and inputting this geometry into the FEA model, it was able to capture these differences.

However, the out-of-plane thickness values are dictated by the quality of the manufacturing process used to produce the original sheet of material, which tends to vary based on location in the sheet. This is not able to be captured in the FEA model. The design stiffness is directly proportional to this stiffness value. Table 3 shows the geometric variations for the in-plane beam thickness and out-of-plane part thickness values for the three prototypes tested.

2) From beams to continuum models.

We have used beam (finite) elements to design the mechanism. Making a continuum model of the beam usually puts some additional material at the intersection of the beams. This can cause additional stiffness. Furthermore, this affects the relative stiffness in X and Y directions, and the location of the center of elasticity.

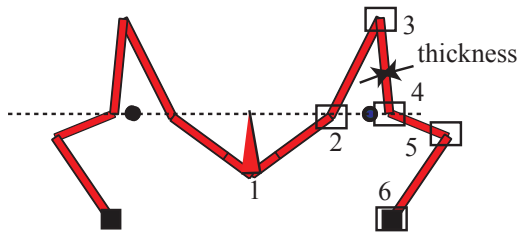*3) Geometry errors from fabrication.*

Figure 16.   SENSITIVITY ANALYSIS FOR THE NODE LOCATIONS.

Pre-stresses in the material can cause errors in the geometry of the fabricated prototypes. Change in the node coordinates, shown in Figure 16, cause an extensive change in the relative $X-$ and $Y-$ stiffness. Table 4 shows that the error in the relative stiffness can be as large as 30% due to just a 10% change of a particular nodal position.

Table 4.   SENSITIVITIES OF THE RELATIVE $X-$ AND $Y-$ STIFFNESS WITH THE NODE LOCATIONS.

Node	% Change in the relative stiffness
2	12
3	30
4	9
5	22
6	20

4) CoE tracking errors.

Tracking the CoE when it is not located at the point of application of the load cell (input) is more difficult (Prototype 2) than when it is at this location (Prototype 1 and 3). In the latter case, the edge of the load cell provides a distinct image feature so it is easier it discern exactly where the load cell pixels end and the pixels at the CoE begin and subsequently track. When the tracking points are not flush with the load cell, the pixels for the CoE become blurred with the surrounding pixels and are harder to extract. Also, since the geometry of the parts after manufacture varies from the nominal values, as stated above, the actual CoE of the part may not be where we estimated it to be a priori. The worst case scenario for when each tracked and fixed points have errors of ± 1 pixel can result stiffness calculation variations of $\pm 20\%$.

5) Experimental setup errors.

The overhead camera used to capture the images during the calibration tests was attached to a rigid vertical support. The camera was assumed to be located in the exact same position when taking pictures of the deformed and undeformed shapes of the prototypes in each calibration test trial. However, each picture was captured manually by depressing the camera shutter as it was mounted to the stand which could have moved the position slightly or caused the plane of the camera not to be exactly parallel to the plane of the prototype being tested. Errors here can result in incorrect displacement data being extracted from the images, yielding stiffness calculation errors.

RECOMMENDATIONS AND CONCLUSIONS

Recommendations for scaling these designs to and implementation at the micro-scale can be drawn from the analysis and observations performed here.

Accurate control of the part geometry, though mircofabrication processes, is required to match theoretical stiffness values with the manufactured device along with CoE positions. Precise measurements of the actual part geometry can be used after fabrication to calculate the CoE and appropriate stiffness values using finite element analysis. Material property tests (tension/compression) to determine the modulus of elasticity for the PDMS parts need to be conducted in order to perform this analysis. The material properties will depend on the manufacturing process steps and should be tested for on a per wafer basis. AFM nanoindentation tests, as described in [5], can be used to verify the device stiffness values calculated from the FEA with the measured part geometry. Care must be taken to ensure proper alignment between the AFM tip and prototype under test to obtain the best results.

When using the test-bed shown in Figure 1, the CCD camera is attached rigidly to the microscope and in the same plane as the workspace. This will ensure a consistent and static focal length for each captured image of the device when in operation. The images are streamed continuously with software so no manual positioning errors during image capture will be encountered. The device itself will need to be installed parallel to the workspace (XY-plane) so that the tracked displacements are truly planar. The image resolution for a particular objective is also known in the microrobotic test-bed, providing accurate pixel:μm ratios. Easily identifiable features should be located at the CoE positions for the best tracking results for these positions. To further reduce tracking (noise) errors, sub-pixel feature tracking or template matching schemes should be employed here. A higher resolution camera could also be used to help increase the accuracy of the force sensor.

In conclusion, we have presented three designs for a decoupled, two-dimensional, vision-based μN force sensor for microrobotic applications. We used the building block approach for conceptual synthesis of the compliant mechanism design for the force sensor. The compliance and stiffness ellipses for the mechanism were constrained to be circles while the magnitudes for the corresponding stiffness and compliance vectors were fixed to zero in order to satisfy the design requirements of decoupled motions along with equal stiffness along the X and Y axes of the mechanism. In the first and last designs, the center of elasticity is at the force input point, while in the second design, it is designed to reside a fixed distance from the input point providing a larger workspace for the object to be manipulated. These designs can be easily scaled up or down and experimental testing of macro-scale prototypes along with finite element analysis was performed to verify the expected behavior for the designs. The observations and analysis here will guide us in our future work of realizing micro-scale, decoupled, two-dimensional, vision-based μN force sensors to be used for microscale robotic manipulation and assembly tasks.

REFERENCES

[1] S. Awtar. *Analysis and Synthesis of Planer Kinematic XY Mechanisms*. PhD thesis, Massachusetts Institute of Technology, Cambridge, MA, USA, 2004.

[2] F. Beyeler, A. Neild, S. Oberti, D. Bell, Y. Sun, J. Dual, and B. Nelson. Monolithically fabricated micro-gripper with integrated force sensor for manipulating micro-objects and biological cells aligned in an ultrasonic field. *IEEE/ASME Journal of Microelectromechanical Systems (JMEMS)*, 16(1):7–15, February 2007.

[3] H.-J. Butt, B. Cappella, and M. Kappl. Force measurements with the atomic force microscope: Technique, interpretation and applications. *Surface Science Reports*, 59:1–152, 2005.

[4] D. Cappelleri. *Flexible Automation of Micro and Meso-Scale Manipulation Tasks with Applications to Manufacturing & Biotechnology*. Ph.d. dissertation, University of Pennsylvania, Philadelphia, PA, August 2008.

[5] D. Cappelleri, G. Piazza, and V. Kumar. Two-dimensional, vision-based μn force sensor for microrobotics. In *Proceedings of IEEE International Conference on Robotics & Automation (ICRA)*, Kobe, Japan, May 2009.

[6] D.J. Cappelleri, J. Fink, B. Mukundakrishnan, V. Kumar, and J.C. Trinkle. Designing open-loop plans for planar micro-manipulation. *IEEE Int. Conf. on Robotics and Automation, Orlando, FL*, May 2006.

[7] P. Cheng, D. Cappelleri, B. Gavrea, and V. Kumar. Planning and control of meso-scale manipulation tasks with uncertainties. In *Proceedings of Robotics: Science and Systems*, Atlanta, GA, USA, June 2007.

[8] N. Ciblak and H. Lipkin. Remote center of compliance reconsidered. In *Proceedings of the ASME International Design Engineering Technical Conferences and Computers and Information in Engineering Conference*. ASME, August 1996.

[9] E. Enikov and B. Nelson. Three-dimensional microfabrication for a multi-degree-of-freedom capacitive force sensor using fibre-chip coupling. *Journal of Micromech. Microeng.*, 10:492–497, 2000.

[10] S. Fatikow and U. Rembold. *Microsystem Technology and Microrobotics*. Springer, New York, 1997.

[11] M. Greminger and B. Nelson. Vision-based force measurement. *IEEE Transactions on Pattern Analysis and Machine Intelligence*, 26(3):290–298, March 2004.

[12] L. Hale. *Principles and techniques for desiging precision machines*. PhD thesis, Massachusetts Institute of Technology, Cambridge, MA, USA, 1999.

[13] A. Hoover and R. Fearing. Rapidly prototyped orthotweezers for automated microassembly. In *IEEE Int. Conf. on Robotics and Automation (ICRA)*, Rome Italy, April 2007.

[14] K.-H. Jeong, C. Keller, and L. Lee. Direct force measurements of biomolecular interactions by nanomechanical force gauge. *Applied Physics Letters*, 86(19), 2005.

[15] C. Kim, Y-M. Moon, and S. Kota. A building block approach to the conceptual synthesis of compliant mechanisms utilizing compliance and stiffness ellipsoids. *Journal of Mechanical Design*, 130(2), February 2008. 022308.

[16] C. J. Kim. Functional characterization of compliant building blocks using eigen-twists and eigen-wrenches. In *Proceedings of the ASME IDETC 2008*, New York, NY, 2008.

[17] S. Koch, G. Thayer, A. Corwin, and M. de Boer. Micromachined piconewton force sensor for biophysics investigations. *Applied Physics Letters*, 89(173901), 2006.

[18] G. Krishnan, C. Kim, and S. Kota. Design synthesis of single point compliant mechanisms utilizing serial concatenation of building blocks. *Submitted to ASME International Design Engineering Technical Conference (IDETC), San Diego, CA*, August-September 2009.

[19] H. Lipkin and T. Patterson. Geometric properties of modelled robot elasticity: Part II, Center-of-Elasticity. In *ASME Design Technical Conferences*, volume DE 45, pages 186–193, Scottsdale, September 1992.

[20] X. Liu, K. Kim, Y. Zhang, and Y. Sun. Nanonewton force sensing and control in microrobotic cell manipulation. In *Proceedings of Robotics: Science and Systems IV*, Zurich, Switzerland, June 2008.

[21] B. Nelson, Y. Zhou, and B. Vikramaditya. Sensor-based microassembly of hybrid MEMS devices. *IEEE Control Systems Magazine*, 18(6):pp. 35 – 45, December 1998.

[22] J. Nevins and D. Whitney. Computer controlled assembly.

[23] F. Sasoglu, A. Bohl, and B. Layton. Design and microfabrication of a high-aspect-ratio pdms microbeam array for parallel nanonewton force measurement and protein printing. *Journal of Micromechanics and Microengineering*, 17:623–632, 2007.

[24] M. Sitti. Teleoperated and automatic nanomanipulation systems using atomic force microscope probes. In 42nd *IEEE Conference on Decision and Control*, Maui, Hawaii USA, December 2003.

[25] Y. Sun and B. Nelson. MEMS for cellular force measurements and molecular detection. *International Journal of Information Acquisition*, 1(1):23–32, 2004.

[26] Y. Sun, B. Nelson, D. Potasek, and E. Enikov. A bulk microfabricated multi-axis capacitive cellular force sensor using transverse comb drives. *Journal Of Micromechanics And Microengineering*, 12(832-840), 2002.

[27] Y. Sun, D. Potasek, D. Piybongkarn, A. Sezen, R. Rajamani, and B. Nelson. Actively servoed multi-axis microforce sensors. In *Proc. 2003 IEEE Int. Conf. on Robotics and Automation, Taipei, Taiwan*, 2003.

[28] J. Thompson and R. Fearing. Automating microassembly with ortho-tweezers and force sensing. In *IEEE/RSJ International Conference on Intelligent Robots and Systems (IROS)*, Maui, HI USA, Oct-Nov 2001.

[29] X. Wang, G.K. Ananthasuresh, and J. Ostrowski. Vision-based sensing of forces in elastic objects. *Sensors and Actuators A*, 94:142–156, 2001.

[30] Y. Yamamoto, R. Konishi, Y. Negishi, and Tatsuo Kawakami. Prototyping ubiquitous micro-manipulation system. In *Proceedings of the IEEE International Conference on Advanced Intelligent Mechatronics (AIM)*, 2003.

[31] X. Zhang. Silicon microsurgery-force sensor based on diffractive optical MEMS encoders. *Sensor Review*, 24(1):37–41, 2004.

[32] X. Zhang, C.-C. Chen, R. Bernstein, S. Zappe, M. Scott, and Olav Solgaard. Microoptical characterization and modeling of positioning forces on drosophila embryos self-assembled in two-dimensional arrays. *Journal of Microelectromechanical Systems*, 14(5):1187–1197, October 2005.

[33] X. Zhang, S. Zappe, R. Bernstein, O. Sahin, C.-C. Chena, M. Fish, M. Scott, and O. Solgaard. Micromachined silicon force sensor based on diffractive optical encoders for characterization of microinjection. *Sensors and Actuators A*, 114:197–203, 2004.

[34] Y. Zhou and B. Nelson. The effect of material properties and gripping force on micrograsping. In *Proceedings of the IEEE International Conference on Robotics & Automation (ICRA)*, San Francisco, CA, April 2000.